Environmental Science and Ecotechnology 18 (2024) 100322

Contents lists available at ScienceDirect

Environmental Science and Ecotechnology

journal homepage: www.journals.elsevier.com/environmental-science-and-ecotechnology/

Original Research

Large-scale land-sea interactions extend ozone pollution duration in coastal cities along northern China

Yanhua Zheng [a], Fei Jiang [a, b, c, *], Shuzhuang Feng [a], Yang Shen [a], Huan Liu [d], Hai Guo [e], Xiaopu Lyu [e], Mengwei Jia [a], Chenxi Lou [a]

[a] Jiangsu Provincial Key Laboratory of Geographic Information Science and Technology, International Institute for Earth System Science, Nanjing University, Nanjing, 210023, China
[b] Jiangsu Center for Collaborative Innovation in Geographical Information Resource Development and Application, Nanjing, 210023, China
[c] Frontiers Science Center for Critical Earth Material Cycling, Nanjing University, Nanjing, 210023, China
[d] School of Environment, Tsinghua University, Beijing, 100084, China
[e] Air Quality Studies, Department of Civil and Environmental Engineering, Hong Kong Polytechnic University, Hong Kong, China

ARTICLE INFO

Article history:
Received 15 December 2022
Received in revised form
21 September 2023
Accepted 23 September 2023

Keywords:
Mongolian high
Source apportionment
WRF-CMAQ
Sea-crossing transport

ABSTRACT

Land-sea atmosphere interaction (LSAI) is one of the important processes affecting ozone (O_3) pollution in coastal areas. The effects of small-scale LSAIs like sea-land breezes have been widely studied. However, it is not fully clear how and to what extent the large-scale LSAIs affect O_3 pollution. Here we explored an O_3 episode to illuminate the role of large-scale LSAIs in O_3 pollution over the Bohai–Yellow Seas and adjacent areas through observations and model simulations. The results show that the northern Bohai Sea's coastal region, influenced by the Mongolian High, initially experienced a typical unimodal diurnal O_3 variation for three days, when O_3 precursors from Beijing–Tianjin–Hebei, Shandong, and Northeast China were transported to the Bohai–Yellow Seas. Photochemical reactions generated O_3 within marine air masses, causing higher O_3 levels over the seas than coastal regions. As the Mongolian High shifted eastward and expanded, southerly winds on its western edge transported O_3-rich marine air masses toward the coast, prolonging pollution for an additional three days and weakening diurnal variations. Subsequently, emissions from the Korean Peninsula and marine shipping significantly affected O_3 levels in the northern Bohai Sea (10.7% and 13.7%, respectively). Notably, Shandong's emissions played a substantial role in both phases (27.5% and 26.1%, respectively). These findings underscore the substantial impact of large-scale LSAIs driven by the Mongolian High on O_3 formation and pollution duration in coastal cities. This insight helps understand and manage O_3 pollution in northern Bohai Sea cities and broadly applies to temperate coastal cities worldwide.

1. Introduction

Ozone (O_3) is a strong oxidising atmospheric gas, recognised as a photochemical pollutant on the surface [1]. As a secondary pollutant, troposphere O_3 is mainly generated by photochemical reactions involving volatile organic compounds (VOCs), methane (CH_4), and carbon monoxide (CO) with the participation of nitrogen oxide (NO_x) [1,2]. Many studies have shown that exposure to ambient O_3 can increase mortality associated with respiratory diseases, chronic obstructive pulmonary disease, cardiovascular diseases, congestive heart failure, and cause damage to vegetation, including agricultural crops [3–8]. In addition, tropospheric O_3 is a prominent greenhouse gas [9]. Since the implementation of the Action Plan on the Prevention and Control of Air Pollution in September 2013, the emission of anthropogenic pollutants in China has been significantly decreased over the past few years [10–14], achieving significant improvements in air quality in China [15,16]. However, ground-level O_3 pollution has increased in many places in China [17–20]. Therefore, a quantitative analysis of the sources of O_3 precursors and the formation process of O_3 is significant to the formulation of air pollution mitigation policies.

* Corresponding author. Jiangsu Provincial Key Laboratory of Geographic Information Science and Technology, International Institute for Earth System Science, Nanjing University, Nanjing, 210023, China.
E-mail address: jiangf@nju.edu.cn (F. Jiang).

https://doi.org/10.1016/j.ese.2023.100322

Ground O_3 concentrations largely depend on emissions and meteorology [21,22]. Natural and anthropogenic emissions provide the precursors for O_3 formation, while meteorology modulates O_3 levels through formation, accumulation, and transport [23]. As dominant O_3 precursors, VOC and NO_x emissions can promote or inhibit O_3 photochemical generation, with the response depending on the proportion of VOCs and NO_x. Generally, urban areas emitted substantial NO_x, leading to O_3 formation being limited by VOC emissions (VOC-limited regime). Conversely, in remote areas, VOC emissions (mainly biogenic VOC) are significantly higher than NO_x, resulting in O_3 formation being limited by NO_x emissions (NO_x-limited regime) [24]. Consequently, O_3 concentrations increase with rising VOC and NO_x emissions in the VOC-limited and NO_x-limited regimes, respectively [25–28].

Previous studies have suggested the importance of meteorological variables such as temperature, relative humidity, and winds to O_3 levels in different regions [21,29,30]. In general, weak winds, high temperatures, low humidity, intense radiation, and clear conditions favour the formation and accumulation of O_3, promoting biogenic VOC emissions and enhancing photochemical O_3 generation [31,32]. Therefore, the corresponding O_3 concentration is usually high [33,34]. The influences of several major weather systems on O_3 levels have also been reported by previous studies. The downdrafts in the periphery of typhoon systems can significantly enhance surface O_3 levels [35–40]. The participation of frontal systems can increase the possibility of pollutant uplift and promote the transboundary transport of O_3 in northern China [41,42]. Greater intensity of the West Pacific subtropical high can cause decreased surface O_3 over South China but increased levels in North China [43]. High-pressure systems during the warm season generally bring higher temperatures, clearer skies, and stagnation, creating favourable conditions for surface O_3 generation [44,45]. In addition, surface O_3 levels are also affected by small-scale circulations such as mountain-valley breezes [46] and sea-land breezes [47,48].

Many O_3 pollution episodes in coastal regions are associated with O_3-rich marine air masses [49]. Marine air masses rich in O_3 are usually related to local and long-range O_3 transport [50]. Land breezes and offshore winds during midnight and the following morning can transport anthropogenic precursors and O_3 to nearshore waters, where photochemical reactions during the day lead to O_3 generation and accumulation [51,52]. In addition, long-range transport from remote lands influenced by large-scale circulations can also cause O_3-rich marine air masses [52–54]. Sea breezes typically appear in the late afternoon, and airflow from outside continental high-pressure systems can deliver marine air masses with rich O_3 generated over the seas to coastal areas, resulting in O_3 pollution [47,48,55]. This problem can be exacerbated where these land-sea atmosphere interactions (LSAIs) are related to severe O_3 episodes [56,57].

The interaction between marine and continental air in China has been a hotspot of coastal air quality research. Many studies have been conducted in Taiwan, Hong Kong, the Pearl River Delta, and the surrounding areas of other South China Sea [47–50,55,58]. The Bohai Sea is China's inland sea, surrounded by the Beijing–Tianjin–Hebei (BTH) region, Shandong, and Liaoning. BTH is one of the most polluted regions in China [59,60]. Shandong Province, adjacent to the Bohai Sea, has the highest air pollutants emissions from its power industry in China, with CO, PM_{10}, $PM_{2.5}$, SO_2, and NO_x emissions from its power plants accounting for 10–11% of total emissions in China [61,62]. Several O_3 pollution events have been reported in the Circum–Bohai–Sea Zone in Liaoning, which may be related to O_3 air masses from the Bohai Sea [63,64]. However, limited studies on the interaction between marine and continental air around the Bohai Sea hinder our understanding of LSAIs in the region.

In this study, we employed the WRF-CMAQ model to simulate an O_3 pollution episode in coastal cities in the northern Bohai Sea from 29 August to 5 September, 2017. This comprehensive analysis includes source apportionment, process analysis, and pollutant transport along the trajectory, ultimately revealing the impact of large-scale LSAIs on this pollution event. The main results are organised as follows: (1) the temporal and spatial variations in O_3 and the evolution of the weather system; (2) the contributions of different physical and chemical processes and geographic pollutant sources to O_3; and (3) the mechanisms of O_3 formation and transport, analysed by selecting representative moments and receptor sites for different O_3 precursor sources.

2. Materials and methods

2.1. Meteorological data and O_3 observations

Hourly surface *in situ* O_3 measurements were obtained from the China National Environmental Monitoring Centre website. The data quality control strictly followed the statistical validity requirements as stated in HJ818-2018 [65]. These quality-controlled O_3 observations were available for 43 cities within the Bohai Rim Region, and we utilised this dataset to evaluate the performance of our model. The target cities for this study included Qinhuangdao, Jinzhou, Yingkou, and Dalian, whose locations are shown in Fig. S1a, each of them having four, five, four, and ten national control urban assessing stations, respectively, in compliance with the China Environmental Protection Standards of HJ664-2013 [66]. These standards specify that sampling ports should be at least 50 m away from stationary sources of pollution and remain unaffected by vehicle emissions. Each urban assessing station represents a spatial scale ranging from at least 500 m to 4 km or from 4 km to tens of kilometres in areas with low pollutant concentrations. To ensure better alignment between the spatial scales represented by the model and the observation sites, we selected one suburban station in each city in this study. The locations of these stations for each city are shown in Fig. S1b. Meteorological data used in this study were downloaded from the National Climate Data Centre. Specifically, 2 m temperature (T_{2m}), 2 m humidity (RH_{2m}), and 10 m wind speed (WS_{10m}) data from 86 stations were selected, mainly located in BTH, Shandong, Northeast China, and central Nei Mongol regions (Fig. S1a). Meteorological observations were taken at 3-h intervals.

2.2. WRF-CMAQ simulation and derivative analysis

The Weather Research and Forecasting (WRF) is a mesoscale numerical weather forecasting model developed by the National Centre for Environmental Protection, the National Centre for Atmospheric Research, and other US scientific research institutions [67]. The Community Multiscale Air Quality (CMAQ) is a regional three-dimensional atmospheric chemistry and transport modelling system developed by the US Environmental Protection Agency [68]. WRF version 4.0 and CMAQ version 5.0.2 were used in this study.

Key configurations of the WRF-CMAQ model included the WRF Single-Moment 6-class scheme for microphysics scheme, the Rapid Radiative Transfer Model for longwave radiation scheme, the Goddard shortwave radiation scheme, the Xu-Randall method for cloud fraction, the Noah Land Surface Model for land surface, the Yonsei University planetary boundary layer (PBL) scheme, the Kain-Fritsch scheme for cumulus parameterisation, AERO6 for aerosol chemistry, and CB05 for gas-phase chemistry. The modelling system consisted of two nested domains, with grid resolutions of 27 km × 27 km and 9 km × 9 km. The outer domain covered most of China and parts of neighbouring countries, while the inner domain

mainly focused on the Bohai Rim Region, including Northeast China, the Korean Peninsula, BTH, Shandong, and central Nei Mongol (Fig. S1a). There were 51 vertical levels for the WRF model, with the top at 50 hPa and 15 levels for the CMAQ model, which were compressed from the WRF levels and had approximately seven levels within the PBL. The WRF model was driven by the final (FNL) operational global analysis data from the National Centre for Environmental Prediction (https://rda.ucar.edu/datasets/ds083.2/, accessed on 7 November, 2020), with a resolution of 1° × 1° and a time interval of 6 h. It should be noted that the default land use data of the WRF model were outdated in China [69]; therefore, the 2017 United States Geological Survey underlying surface classification data (https://lpdaac.usgs.gov/products/mcd12c1v006, accessed on 7 December, 2018) were applied to reduce the simulation errors in this study. The WRF-CMAQ model was executed from 25 August to 5 September, 2017, with the initial four days considered as spin-up runs.

Biogenic emissions were calculated offline using the Model of Emissions of Gases and Aerosols from Nature (MEGAN) version 2.04 [70]. The anthropogenic emission inventory was obtained from the 2017 Multi-resolution Emission Inventory for China (MEIC2017; http://meicmodel.org/, accessed on March 24, 2021) [14,71], which has a resolution of 0.25° × 0.25°. The MEIC2017 inventory covers emission sectors of industry, power, transportation, residential, and agriculture, and major atmospheric pollutants, such as SO_2, NO_x, CO, non-methane volatile organic compounds, NH_3, CO_2, $PM_{2.5}$, PM_{10}, black carbon, and organic carbon. Anthropogenic emissions outside China were obtained from the mosaic Asian anthropogenic emission inventory [72]. In addition, we use the marine shipping emission inventory in East Asia, derived from the Shipping Emission Inventory Model developed by Tsinghua University, based on high Precision Automatic Ship Identification System data [73–75]. This currently provides annual ship emissions for East Asia in 2017, with a grid spacing of 0.1°, covering SO_2, NO_x, CO, non-methane volatile organic compounds, $PM_{2.5}$, black carbon, and organic carbon [76].

The Integrated Process Rate (IPR) analysis within the process analysis module can quantify grid-scale individual contributions to specific species' concentrations from advection, diffusion, emissions, dry deposition, aerosol and cloud processes, and chemical processes [77]. The IPR analysis has been widely applied to investigate pollution formation mechanisms, such as O_3 and particulate matter [78–83]. This work applied the IPR analysis embedded in the CMAQ model to investigate individual O_3 contributions at each time step during the simulation.

The Integrated Source Apportionment Method coupling in the CMAQ model (CMAQ-ISAM) calculates source attribution for O_3 and particulate matter. It has been verified as an effective tool for identifying emission contributions from regions and sectors [84–89]. In this study, CMAQ-ISAM was applied to estimate the source contributions to O_3, running only within the outer domain. Anthropogenic emissions from seven regions were tagged: BTH, Shandong, Nei Mongol, Northeast China, Japan, the Korean Peninsula, and the ocean. ISAM also tracks three additional contributions: initial conditions, boundary conditions, and non-tagged emissions, combined as background contributions in this study.

2.3. HYSPLIT simulation

The Hybrid Single-Particle Lagrangian Integrated Trajectory (HYSPLIT) model can compute trajectories of air parcels and simulate dispersion, chemical transformation, and deposition [90,91]. The HYSPLIT model is widely used to detect the transportation trajectories of air pollution. Here, driven by the hourly WRF output, HYSPLIT 4.8 was conducted to track air masses arriving 50 m above the four receptor cities. The trajectories of every 6 h during the study period were calculated, and each trajectory lasted 144 h.

3. Results and discussion

3.1. Characteristics of meteorological factors and O_3 observations

We first analysed the hourly variation of meteorological conditions in the four cities. Generally, meteorological factors exhibited similar variations in the four cities during the study period (Fig. S2). From 29 August to 5 September, T_{2m} showed a slight overall increase, with weaker daily variations in Dalian than the other three cities. This difference can be attributed to Dalian's coastal location, where temperature was regulated by the sea. On 29 August, RH_{2m} was relatively low and then gradually increased. After 31 August, RH_{2m} reached its highest level and remained stable, except in Jinzhou, where RH_{2m} decreased significantly on 5 September. The variations in WS_{10m} were similar in the four cities. From 29 to 30 August, WS_{10m} was relatively high, while from 31 August to 2 September, it decreased to below 4 m s^{-1} overall. After 3 September, the wind speed increased again. Similar temporal patterns of O_3 mixing ratios were also observed in the four cities (Fig. 1a). During the initial two days, O_3 mixing ratios remained relatively low, with daily maximum hourly mixing ratios (DMHMR) staying below the level II threshold (approximately 75 ppb) for hourly mean O_3 mixing ratios according to the Ambient Air Quality Standard (GB3095-2012) [92]. The DMHMR exceeded the threshold starting from 31 August. Over the following three days, O_3 mixing ratios exhibited a significant unimodal variation, with the highest levels in the afternoon (approximately 14:00 LT) and the lowest in the early morning (approximately 06:00 LT). This diurnal variation is a characteristic feature of O_3 pollution days and has been reported in many previous studies [39,82,93,94]. After 3 September, the diurnal amplitude of O_3 mixing ratios changed significantly, with the DMHMR comparable to the previous days but the nighttime mixing ratios significantly higher than those of the previous three days. We validated the model performance by comparing the simulated hourly meteorological variables and O_3 mixing ratios with available surface observations (Section 2.1). Overall, the WRF-CMAQ model reproduced the variations of meteorological factors and O_3 mixing ratios well in this study (see Text S1–S2, Figs. S2–S3, Table S1 in the Supplementary Materials).

According to these pollution characteristics, we divide the entire O_3 pollution episode (days with DMHMR higher than 75 ppb) into two stages: Phase I (31 August to 2 September) and Phase II (3–5 September). In Fig. 1b and c, we depict the simulated spatial distributions of mean sea-level pressures and wind fields 10 m above ground level during Phase I and Phase II, respectively. Clearly, this pollution episode occurred during the eastward movement of a continental high pressure, commonly referred to as the Mongolian High in East Asia. From Phase I to Phase II, the Mongolian High moved east and expanded. During Phase I, the centre of the Mongolian High was located between the Yellow Sea and the Bohai Sea. During the daytime (08:00–19:00 LT), regions such as Shandong, BTH, Northeast China, central Nei Mongol, and the Korean Peninsula were controlled by the Mongolian High. During this period, winds were weak (below 3 m s^{-1}), and the weather conditions were stable (Fig. 1b), favouring photochemical O_3 generation. Consequently, these regions exhibited high O_3 mixing ratios, with a mean mixing ratio exceeding 60 ppb (Fig. 1e). At night (20:00–07:00 LT), the O_3 in these regions was consumed through NO_x titration, making significantly lower O_3 mixing ratios compared to daytime (Fig. 1d). Except for some remote regions like northern BTH, O_3 mixing ratios decreased to below 45 ppb in most areas. O_3 mixing ratios over the

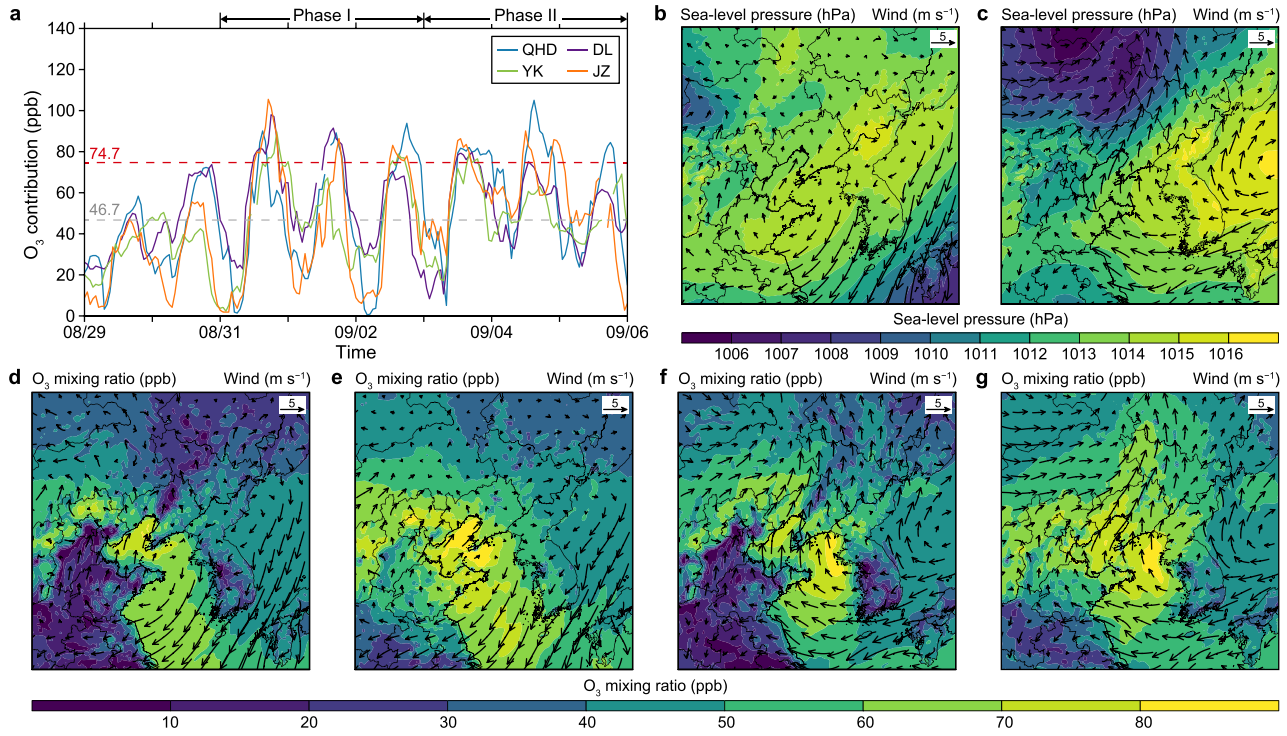

Fig. 1. **a**, Hourly O_3 mixing ratios measured in the four cities from 29 August to 5 September, 2017. QHD: Qinhuangdao, JZ: Jinzhou, YK: Yingkou, DL: Dalian. The grey and red dotted horizontal lines represent the China Ambient Air Quality Standard (GB3095-2012) level I and level II, respectively. **b**–**c**, Mean surface simulated sea-level pressure (hPa) during Phase I (**b**) and Phase II (**c**). **d**–**e**, Mean surface simulated O_3 mixing ratios during 20:00–07:00 LT (**d**) and 08:00–19:00 LT (**e**) during Phase I. **f**–**g**, Mean surface simulated O_3 mixing ratios during 20:00–07:00 LT (**f**) and 08:00–19:00 LT (**g**) during Phase II. The arrows in panels **b**–**g** represent the winds at 10 m above ground level.

Bohai Sea, Yellow Sea, and East China Sea were notably high, exceeding 60 ppb in most sea areas and reaching over 80 ppb in the Bohai Sea. The Bohai Sea was affected by southeast winds, while the Yellow Sea was controlled by the northeast winds, indicating the transport of precursors from the Korean Peninsula to the Yellow Sea and from Shandong to the Bohai Sea. Even during night-time, O_3 mixing ratios over these bodies of water remained high, surpassing those in remote regions due to lower NO_x emissions and weak O_3 deposition over water surfaces.

In Phase II, the centre of the Mongolian High moved to the Sea of Japan, placing the Yellow Sea, the Bohai Sea, and surrounding regions west of the Mongolian High. During this phase, the Yellow Sea was predominantly affected by easterly and south-easterly winds, while the Bohai Sea was still influenced by south-westerly winds (Fig. 1c). O_3 from the Yellow Sea was transported to Shandong and the northern coastal regions due to the southeast wind, while O_3 from the Bohai Sea affected Liaoning and BTH under the influence of the southwest wind. Throughout these days, O_3 mixing ratios remained high in land. In contrast to Phase I, O_3-rich air masses shifted northward, resulting in O_3 mixing ratios exceeding 60 ppb in Nei Mongol, the northern Korean Peninsula, and Northeast China (Fig. 1g). O_3 pollution in other land regions was similar to that in Phase I. At night, the northward movement of O_3-rich air masses was more obvious without the influence of photochemical reactions (Fig. 1f). At this time, under the action of the southwest wind, Nei Mongol, northern BTH, western and southern Liaoning were affected by O_3 transport, leading to O_3 mixing ratios above 60 ppb. In this phase, O_3 pollution was severe over the Yellow Sea and the Bohai Sea, with maximum mixing ratios exceeding 80 ppb. O_3 pollution over the East China Sea decreased because of the northward movement of O_3-rich air masses.

3.2. Process analysis

In order to understand the formation processes of O_3, the IPR analysis described in section 2.2 was used to quantify the contributions of the chemical process, cloud process, dry deposition, horizontal and vertical advections, and horizontal and vertical diffusions to the variations of O_3 mixing ratios at each model grid. Fig. 2 shows the mean surface O_3 mixing ratios and O_3 contributions from each process at the bottom level and different altitudes in Phase I and Phase II. It is important to note that O_3 consumed by surface dry deposition is continuously compensated by vertical diffusion, so we combined their contributions. The mean surface O_3 mixing ratio in Phase II (57 ppb) was higher than in Phase I (46 ppb), consistent with the previous conclusion. The average contribution of the cloud process with aqueous chemistry and horizontal diffusion contributed little to O_3, with an average within ±0.5 ppb. Photochemistry consumed O_3 in both phases, with average contributions of −21 and −24 ppb, respectively, and the difference between the two phases was only 3 ppb. Vertical diffusion accounted for most O_3 after compensating for dry deposition in both phases. The total contributions of vertical diffusion and dry deposition in Phase I and Phase II were 18 and 22 ppb, respectively.

The difference in O_3 mixing ratios between the two phases primarily stemmed from horizontal and vertical advection. Compared with Phase I, the contribution of horizontal advection to O_3 in Phase II was greater and increased from 9 to 18 ppb. The contribution of vertical advection decreased from −5 to −17 ppb, indicating that the upsurge outside the continental high-pressure system transported more O_3 from the lower air to the upper air in Phase II. Examining the vertical distribution of ozone contribution, O_3 mixing ratios peaked at 72 ppb at 500 m in Phase I and

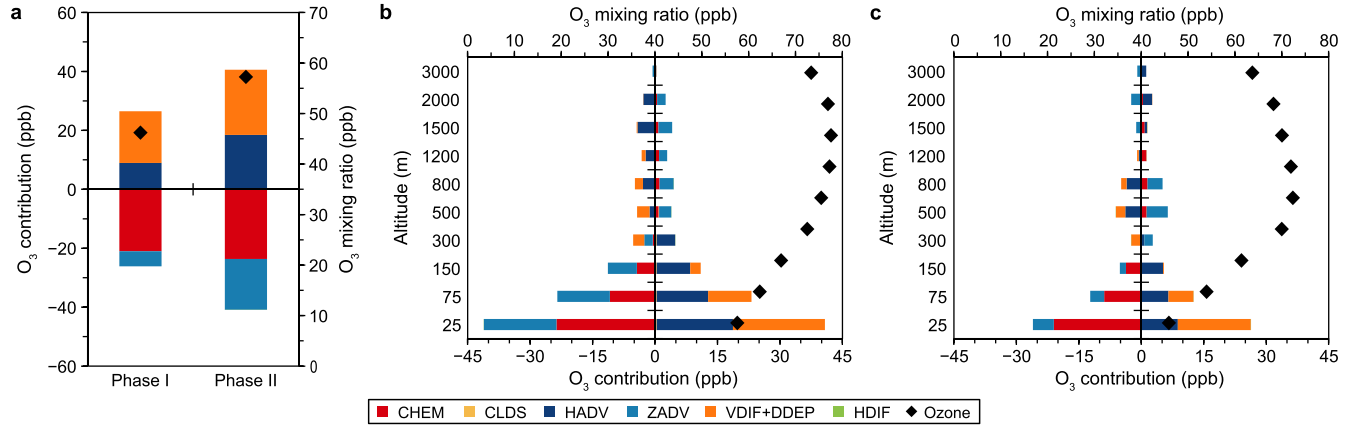

Fig. 2. Contributions of physical and chemical processes to O_3 formation and O_3 mixing ratios at the bottom level (**a**), and at different altitudes in Phase I (**b**) and Phase II (**c**). Ozone: total O_3 mixing ratio; CHEM: chemical process; CLDS: cloud process; HADV: horizontal advection; ZADV: vertical advection; VDIF + DDEP: vertical diffusion and dry deposition; HDIF: horizontal diffusion.

78 ppb at 1200 m in Phase II. In both phases, O_3 was horizontally transported inward at low altitudes and outward at high altitudes, while vertical transport occurred from the lower layers below 300 m to the middle and high layers due to updraft. However, compared to Phase I, the transports were stronger in both horizontal and vertical directions in Phase II. These analyses indicate that the increased contribution from the horizontal advection contribution was the dominant factor driving O_3 pollution in Phase II.

3.3. O_3 contributions from different regions

3.3.1. Hourly O_3 source apportionment in the four cities

Fig. 3 displays the hourly O_3 contributions of the emissions from various regions, including BTH, Northeast China, Shandong, Nei Mongol, the Korean Peninsula, and Japan, to O_3 mixing ratios in the four cities during the O_3 episode (Phase I and II). The sources of O_3 in the four cities exhibited significant differences between different phases, and even within the same phase, the sources of O_3 differed across different cities. The background contribution remained relatively stable across different cities and phases, accounting for approximately one-third of the total contribution. Since Qinhuangdao is located in the BTH region, while the other cities are located in Northeast China, the contributions of BTH emissions to Qinhuangdao and the contributions of Northeast China to Yingkou, Jinzhou, and Dalian represented their respective local contributions. In Qinhuangdao, the local contribution dominated on 31 August (more than 60%), and then it gradually weakened, reaching its lowest level on 4 September (less than 5%) and strengthening again on 5 September. In Yingkou, Jinzhou, and Dalian, the local and BTH's contributions were comparable on 31 August, with contributions from other regions being negligible. From 1 to 5 September, the local and BTH's contributions showed a significant downward trend, while the contribution from Shandong increased significantly, especially in Dalian, with the maximum hourly contribution reaching 49 ppb at 16:00 LT on 1 September, which accounted for 52.4% of the O_3 concentration at that time. From 31 August to 1 September, the sea contribution was weak and mainly occurred in the afternoon and night. However, after the afternoon of 2 September, it increased significantly and remained high, with contribution rates above 10% for most of the time and reaching 30% in Dalian at 21:00 LT on 3 September. The contribution from the Korean Peninsula was negligible from 31 August to 3 September. However, it increased significantly starting from 4 September, especially in the evening of 4 September and the early morning of 5 September, with the largest hourly contributions to Qinhuangdao, Jinzhou, Yingkou, and Dalian of 28.0%, 29.6%, 37.8%, and 44.5%, respectively.

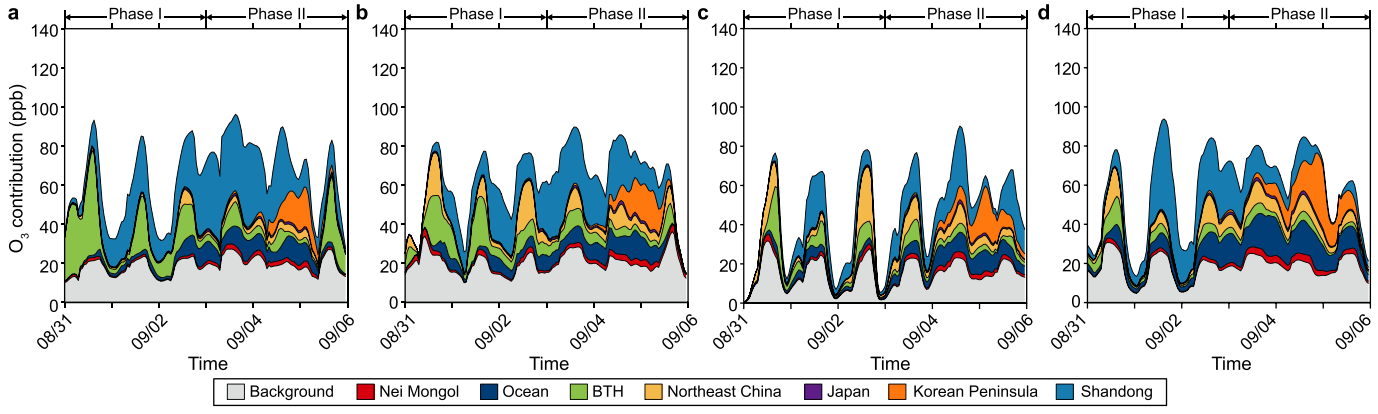

Fig. 3. Time series of contributions from different regions to O_3 mixing ratios during the two phases in Qinhuangdao (**a**), Jinzhou (**b**), Yingkou (**c**), and Dalian (**d**).

Table 1
Mean O_3 contribution from different source regions during Phase I and II (%). (QHD: Qinghuangdao, JZ: Jinzhou, YK: Yingkou, DL: Dalian, BTH: Beijing–Tianjin–Hebei region).

Period	City	BTH	Northeast China	Japan	Shandong	Korean Peninsula	Nei Mongol	Ocean	Background
Phase I	QHD	28.0	2.6	0.8	31.1	0.6	1.7	5.4	29.9
	JZ	18.4	12.8	0.8	23.8	0.7	3.0	7.1	33.4
	YK	15.0	17.0	0.9	20.2	0.7	3.0	6.5	36.7
	DL	8.5	9.7	1.0	34.9	0.8	2.1	11.3	31.8
	Average	**17.5**	**10.5**	**0.9**	**27.5**	**0.7**	**2.5**	**7.6**	**33.0**
Phase II	QHD	10.2	3.7	1.2	35.8	7.7	2.7	10.2	28.5
	JZ	7.3	7.2	1.4	28.9	8.7	3.6	11.0	31.9
	YK	6.8	9.4	1.6	25.2	11.3	3.6	13.2	29.0
	DL	4.7	9.2	1.8	14.4	15.2	4.2	20.5	30.1
	Average	**7.3**	**7.4**	**1.5**	**26.1**	**10.7**	**3.5**	**13.7**	**29.9**

On average, during Phase I, in Qinhuangdao, the contributions from BTH, Shandong, and the background were comparable, accounting for approximately 30% (Table 1). In Jinzhou, Yingkou, and Dalian, apart from the background, emissions from Shandong had the largest contribution (26%), while the contributions from local emissions (i.e., Northeast China) and BTH were comparable (13.2% vs. 14.0%). O_3 contributions from the ocean accounted for 7.6%, whereas those from Japan, the Korean Peninsula, and Nei Mongol were minimal. In Phase II, compared to Phase I, the local contributions were reduced in all four cities. In Qinhuangdao, it reduced from 28.0% to 10.2%; in the other cities, it even decreased to below 10%. The contribution from Shandong remained significant, ranging from 14.4% to 35.8%, with an average percentage of 26.1%. Except for Dalian, the contribution from Shandong further increased. It is noticeable that the contributions from the ocean and the Korean Peninsula increased significantly, with average percentages of 13.7% and 10.7%, respectively. Overall, apart from the background contribution, the nonlocal contribution increased from around 50% in Phase I to more than 60% in Phase II, especially the contribution of cross-sea transmission (i.e., Shandong, the Korean Peninsula, Japan, and the ocean), which increased from around 30% to more than 50%.

3.3.2. *Spatial distribution of the mean O_3 contributions*

The spatial distributions of the mean O_3 contributions from different regions in Phase I and II are shown in Fig. 4. In Phase I, the contribution from BTH was mainly observed in the western and northern parts of BTH, as well as in the neighbouring northern Nei Mongol and western Liaoning, with maximum contributions exceeding 30 ppb. In addition, the influence of BTH on O_3 extended to the Bohai Sea, the Yellow Sea and the East China Sea, with maximum contributions of approximately 6 ppb. The contribution from Northeast China exhibited a relatively wide distribution and, apart from affecting Northeast China itself, also made a significant contribution to the Korean Peninsula and the Yellow Sea. The largest contribution of approximately 15 ppb was found over the Yellow Sea, surpassing even the contributions from Northeast China. In Phase I, the O_3 contribution from Shandong was mainly concentrated in the Bohai Sea and its surrounding coastal regions, gradually decreasing from the sea to the inland areas, with maximum contributions of over 30 ppb. The O_3 contribution from the Korean Peninsula was mainly distributed in the Yellow Sea, the East China Sea, and their coastal areas, with minimal contribution to the northern Bohai Sea. The O_3 contribution from the ocean mainly affected the seas and their coastal regions, with maximum contributions of 10–15 ppb. During Phase I, the Mongolian High was centred between the Yellow Sea and the Bohai Sea (Fig. 1b). Consequently, the Bohai Sea was influenced by the southeast wind, while the northeast wind prevailed over the Yellow Sea. Considering the distribution of contributions from each source region, a process of precursor transport from land to sea was observed. For instance, the southwest wind transported precursors from Shandong to the Bohai Sea, while the northeast wind transported precursors from the eastern provinces to the Yellow Sea.

In Phase II, due to the changes in wind direction and increased wind speed, the contribution from each region shifted northward, leading to an expanded spatial coverage of their impact. For example, under the influence of the southwest wind, the O_3 contribution from BTH to Nei Mongol increased, while its contribution in BTH, Liaoning and the Yellow Sea decreased. The O_3 contribution from Shandong to Northeast China increased, while its contribution to the Bohai Sea decreased. In particular, the contribution from the Korean Peninsula increased significantly not only in the Yellow Sea, with maximum contributions exceeding 30 ppb, but also over the Bohai Sea, its coastal areas, and Northeast China. In addition, it was found that although both BTH and Northeast China were controlled by southwesterly winds, they still made substantial contributions to the Bohai Sea and the Yellow Sea (upwind areas). This phenomenon may be attributed to the transport of precursors delivered to these regions in Phase I.

The total ozone contribution from the source regions of BTH and Northeast China Phase II is presented in Fig. 4f and g. To evaluate the contribution caused by the return of precursors after marine transport, a sensitivity experiment was conducted. In this case, the emissions from these two source regions in Phase II were turned off, while their emissions from Phase I were retained. The emissions from other source regions remained unchanged. The ISAM model was then run again to characterise the lag in ozone contribution from these two source regions due to marine transport. The distribution results are shown in Fig. 4k, l. The emissions from BTH and Northeast China in Phase I significantly contributed to O_3 over the Bohai Sea, the Yellow Sea, and their surrounding areas, ranging 2–6 ppb. This indicates that the precursors emitted from these two source regions in Phase I were transported to the seas under the influence of the offshore winds, where O_3 was formed, and then returned to the coastal areas after the wind direction changed in Phase II. Transport from the sea resulted in the re-influence of precursors emitted in Phase I on ozone levels in coastal cities again after a few days, thereby sustaining ozone levels high in Phase II. In other words, large-scale LSAIs helped to prolong the duration of O_3 pollution.

3.4. *Formation and transport of O_3 along the movements of air masses*

To gain further insight into the formation and transport processes of O_3 in Phase II, we analysed the variations in vertical O_3 and NO_x mixing ratios, as well as the chemical generation and consumption of O_3 within the air masses along the trajectories. Three typical examples are shown in Fig. 5.

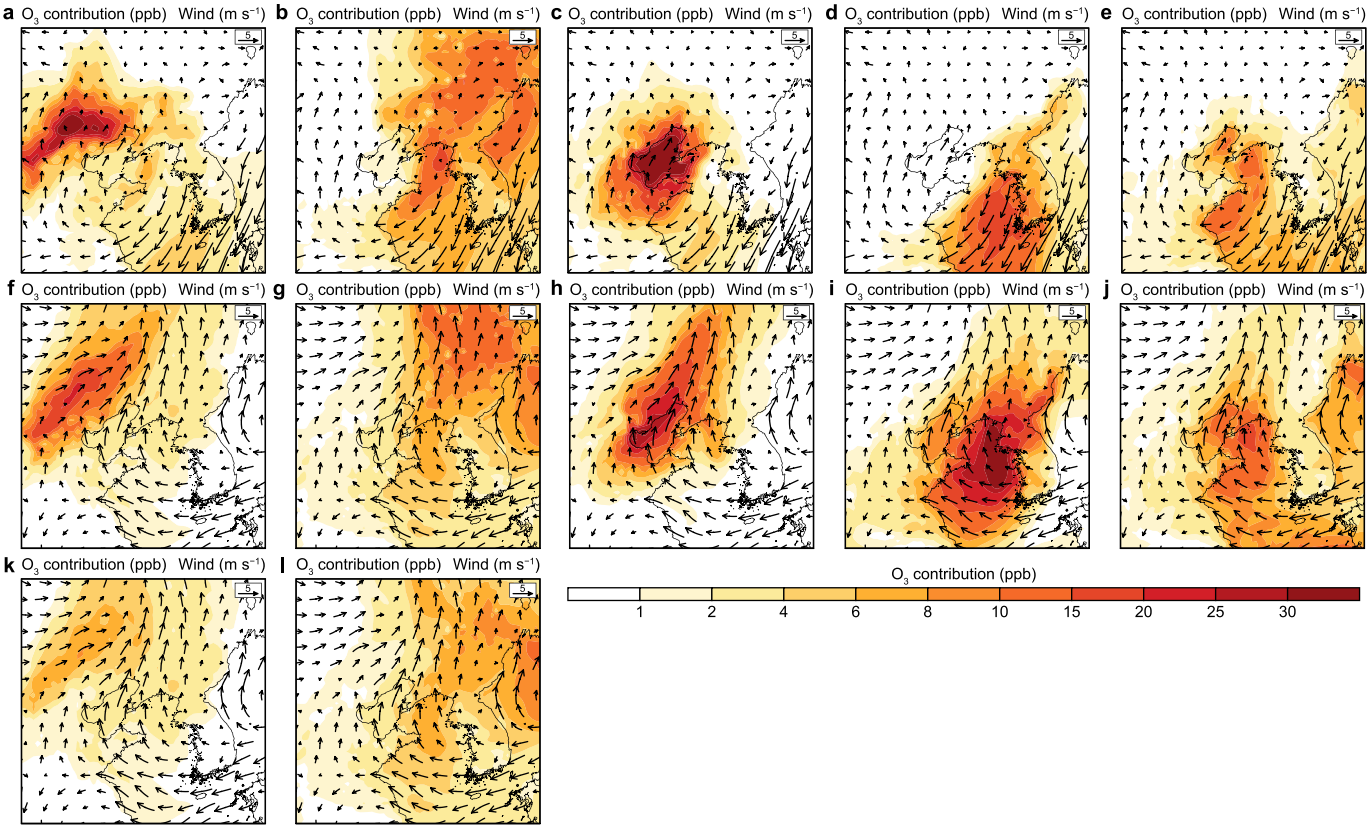

Fig. 4. **a**–**e**, Distribution of mean O_3 contributions in Phase I from BTH (**a**), Northeast China (**b**), Shandong (**c**), the Korean Peninsula (**d**), and the ocean (**e**). **f**–**j**, Distribution of mean O_3 contributions in Phase II from BTH (**f**), Northeast China (**g**), Shandong (**h**), the Korean Peninsula (**i**), and the ocean (**j**). **k**–**l**, Mean O_3 contributions in Phase II from emissions emitted only during Phase I in BTH (**k**) and Northeast China (**l**).

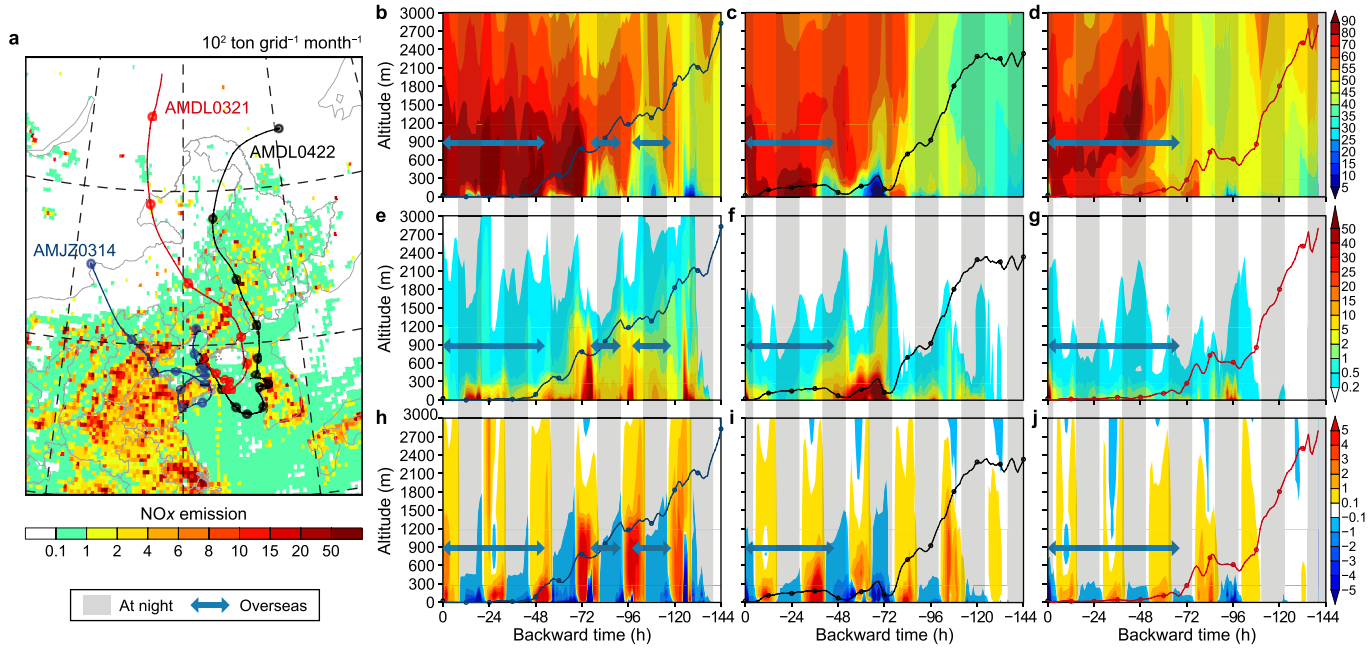

Fig. 5. **a**, 144-h horizontal backward trajectories of the air mass reaching Jinzhou at 14:00 LT on 3 September, Dalian at 22:00 LT on 4 September, and Dalian at 21:00 on 3 September (shaded represent NO_x total emission in September). The vertical O_3 mixing ratios along AMJZ0314 (**b**), AMDL0422 (**c**), AMDL0321 (**d**), NO_x mixing ratios along AMJZ0314 (**e**), AMDL0422 (**f**), AMDL0321 (**g**), and O_3 from chemical processes along AMJZ0314 (**h**), AMDL0422 (**i**), AMDL0321 (**j**). Black lines represent the backward trajectories in the horizontal and vertical directions, thick blue lines with arrows represent the air mass moving across the seas, and grey translucent rectangles denote the night-time.

3.4.1. Example 1: transport through BTH, the Bohai Sea, the Shandong peninsula, and then return to coastal cities

We selected the air mass arriving in Jinzhou at 14:00 LT on 3 September as an example and named it AMJZ0314 (Fig. 5a, b, e, h). The air mass entered the high-emission regions of BTH in the early morning of 29 August, passed through the Bohai Sea between BTH and the Shandong Peninsula in the afternoon of 29 August, and reached the Shandong Peninsula on 30 August. After a slow turn around the Shandong Peninsula, it returned to the Bohai Sea on the night of 1 September, stayed near the Liaodong Peninsula for approximately one and a half days, crossed the Bohai Sea, and finally reached Jinzhou at 14:00 LT on 3 September.

During this period, as the air mass passed through the BTH region and the Shandong peninsula, the NO_x mixing ratios increased significantly, resulting in significant photochemical O_3 generation in these regions. When passing through the BTH region, O_3 mixing ratios in the air mass rose to more than 55 ppb. Upon passing through the Bohai Sea for the first time, they decreased significantly due to NO_x titration. However, when it reached the Shandong peninsula and completed a turnaround for one day and a half, O_3 mixing ratios increased to 90 ppb. After the air mass moved to the Bohai Sea for the second time on 31 August, the NO_x mixing ratios decreased, and the generation and O_3 consumption were reduced. In the following three days, although there was some consumption near the ground at night, O_3 mixing ratios at altitudes of 200−1200 m remained above 80 ppb. In addition, it could also be found that O_3 could be further generated through photochemical reactions during movement over the Bohai Sea. This clearly reveals the important impact of emissions from the Shandong peninsula on O_3 mixing ratios in northern Bohai cities.

3.4.2. Example 2: transport from northeast China passes through the Korean Peninsula and the seas and then reaches coastal cities

We selected the air mass arriving in Dalian at 22:00 on 4 September, when the contribution from the Korean Peninsula was most significant, as the second example, denoted as AMDL0422 (Fig. 5a, c, f, i). During the six-day movement before arriving in Dalian at 22:00 on 4 September, the air mass quickly passed through Northeast China from north to south, slowly passed through the Korean Peninsula, and then entered the Yellow Sea in the southern part of the Korean Peninsula on the night of 2 September. It then moved from south to north, crossed the Yellow Sea, and reached Dalian. In the Korean Peninsula, the air mass slowly passed through Pyongyang and then Seoul. Particularly, when passing through Seoul, the NO_x mixing ratios increased significantly (more than 40 ppb). In Northeast China, O_3 mixing ratios in the air mass were very low (less than 40 ppb). When passing through North Korea, there was a certain increase in O_3 mixing ratios (approximately 45 ppb), and upon entering South Korea, O_3 mixing ratios further increased, especially near Seoul. Although near the ground, O_3 mixing ratios were depleted due to high NO_x mixing ratios, in the middle layer of the PBL, they reached more than 60 ppb. After the air mass entered the Yellow Sea, the mixing ratios in the upper and middle layers of the PBL remained above 60 ppb. Although the NO_x mixing ratios near the ground dropped to 2−5 ppb, the photochemical O_3 generation further strengthened, making O_3 mixing ratios near the ground reach more than 90 ppb. At night on 3 September, due to the decrease in NO_x mixing ratios in the air mass, titration was weakened, and the O_3 decrease was not significant. On 4 September, due to the decrease in NO_x mixing ratios, O_3 mixing ratios and photochemical O_3 contributions were lower than those on 3 September. When the air mass reached Dalian at night, local NO_x participated in titration reactions, depleting O_3 and reducing O_3 mixing ratios to approximately 70 ppb.

3.4.3. Example 3: transport from Nei Mongol and northeast China to the Yellow Sea and then return to coastal cities

We examine a specific air mass event, denoted as AMDL0321, arriving in Dalian at 21:00 LST on 3 September (Fig. 5a, d, h, j). At this moment, the contribution from the ocean was the most significant during this O_3 episode in Dalian (Fig. 3). It was noteworthy that when it's more than 140 h, the trajectory of this air mass could not be calculated, as it extended beyond the domain of the WRF simulation, rendering it missing data. The air mass entered China on 29 August and traversed through Nei Mongol, Liaoning, and the northern Korean Peninsula before reaching the Yellow Sea on the night of 31 August. It then moved slowly over the Yellow Sea for approximately three days before reaching Dalian. When the air mass was in China, O_3 mixing ratios did not change much and were always approximately 45 ppb. When passing through the northern Korean Peninsula, there was a certain increase in O_3 mixing ratios in the lower PBL, subsequently reverting to approximately 50 ppb. From 1 to 3 September, the air mass resided over the Yellow Sea. Influenced by marine emissions, near-surface NO_x mixing ratios remained in the range of 1−2 ppb. O_3 was generated by photochemical reactions during the day, with relatively weak consumption occurring at night. Consequently, there was a gradual increase in O_3 mixing ratios in the air mass, especially at altitudes ranging from 1200 to 1500 m. On 3 September, O_3 mixing ratios of the air mass rose to 80 ppb. As the air mass approached Dalian, the NO_x mixing ratios soared under the influence of local emissions, while O_3 mixing ratios near the ground decreased slightly due to titration and deposition.

4. Conclusions

In this study, we examined an O_3 pollution episode occurring in coastal cities located in the northern Bohai Sea from 29 August to 5 September, 2017. To gain insights into this event, we employed the WRF-CMAQ and HYSPLIT models alongside source apportionment, process analysis, and transport analysis along the trajectories. Our investigation revealed the impact of large-scale LSAIs on this pollution event.

The ozone pollution episode has been confirmed to follow a two-stage process. During the first stage, influenced by the Mongolian High, land-based precursors (primarily originating from Shandong, BTH, and Northeast China) were transported over the Yellow Sea and the Bohai Sea via northward winds. In these regions, O_3 was generated through photochemical reactions and subsequently accumulated due to weak titration and deposition mechanisms. In the second stage, as the Mongolian High shifted eastward and expanded, southerly flows at its western edge transported O_3-rich marine air masses back to the coast. This phenomenon prolonged the duration of pollution by three days, although it resulted in weaker diurnal variations in O_3 levels.

Throughout the episode, emissions from Shandong made significant contributions to ozone levels in coastal cities during both stages. In the first stage, local emissions from BTH and Northeast China played a substantial role (28% in total). In the second stage, the overall local contribution (14.7% in total) decreased significantly, while precursors from the Korean Peninsula (10.7%) and marine shipping (13.7%) had notable impacts.

The investigations reveal that the large-scale LSAIs driven by the Mongolian High could influence the O_3 formation and distribution in coastal cities, as well as prolong the pollution duration. These

findings hold considerable importance for the understanding and control of O_3 pollution in coastal cities.

CRediT authorship contribution statement

Yanhua Zheng: Investigation, Software, Validation, Visualization, Formal Analysis, Writing - Original Draft, Writing - Review & Editing. **Fei Jiang:** Conceptualization, Methodology, Funding Acquisition, Formal Analysis, Writing - Review & Editing. **Shuzhuang Feng:** Data Curation. **Yang Shen:** Visualization. **Huan Liu:** Resources. **Hai Guo:** Supervision. **Xiaopu Lyu:** Supervision. **Mengwei Jia:** Formal Analysis. **Chenxi Lou:** Formal Analysis.

Data availability

The meteorological data can be accessed from the National Climate Data Centre (NCDC) at http://www.ncdc.noaa.gov/oa/ncdc.html. Hourly surface *in situ* O_3 measurements can be accessed from the website of the China National Environmental Monitoring Station. The anthropogenic emission inventory can be accessed from the 2016 Multi-resolution Emission Inventory for China from http://meicmodel.org/. The data and related codes of this study are available to the community and can be accessed upon request from Fei Jiang (jiangf@nju.edu.cn) at Nanjing University. We would like to share our data and results with the scientific community at the https://doi.org/10.5281/zenodo.6997487 website.

Code availability

The source codes for the analysis of this study are available from the corresponding author Fei Jiang: jiangf@nju.edu.cn.

Declaration of competing interests

The authors declare that they have no known competing financial interests or personal relationships that could have appeared to influence the work reported in this paper.

Acknowledgments

This work is supported by the National Key Research and Development Program of China (Grant No: 2022YFC3703505) and the Research Funds for the Frontiers Science Center for Critical Earth Material Cycling, Nanjing University (Grant No: 090414380031). The authors also gratefully acknowledge the High-Performance Computing Center (HPCC) of Nanjing University for performing the numerical calculations in this paper on its blade cluster system. We would like to thank the China National Environmental Monitoring Station for making the hourly surface O_3 mixing ratio observations available and NOAA's National Centers for Environmental Information for providing the meteorological data (http://www.ncdc.noaa.gov/oa/ncdc.html). The NCAR and EPA made the WRF and CMAQ models available, and we gratefully acknowledge them. Additionally, we also thank the MEIC team for providing the anthropogenic emissions (http://www.meicmodel.org/).

Appendix A. Supplementary data

Supplementary data to this article can be found online at https://doi.org/10.1016/j.ese.2023.100322.

References

[1] P.S. Monks, A.T. Archibald, A. Colette, O. Cooper, M. Coyle, R. Derwent, D. Fowler, C. Granier, K.S. Law, G.E. Mills, D.S. Stevenson, O. Tarasova, V. Thouret, E. von Schneidemesser, R. Sommariva, O. Wild, M.L. Williams, Tropospheric ozone and its precursors from the urban to the global scale from air quality to short-lived climate forcer, Atmos. Chem. Phys. 15 (15) (2015) 8889–8973, https://doi.org/10.5194/acp-15-8889-2015.

[2] P.S. Monks, Gas-phase radical chemistry in the troposphere, Chem. Soc. Rev. 34 (5) (2005) 376–395, https://doi.org/10.1039/B307982C.

[3] H.Z. Sun, P. Yu, C. Lan, M.W.L. Wan, S. Hickman, J. Murulitharan, H. Shen, L. Yuan, Y. Guo, A.T. Archibald, Cohort-based long-term ozone exposure-associated mortality risks with adjusted metrics: a systematic review and meta-analysis, Innovation 3 (3) (2022) 100246, https://doi.org/10.1016/j.xinn.2022.100246.

[4] V. Bermejo, B.S. Gimeno, J. Sanz, D. de la Torre, J.M. Gil, Assessment of the ozone sensitivity of 22 native plant species from Mediterranean annual pastures based on visible injury, Atmos. Environ. 37 (33) (2003) 4667–4677, https://doi.org/10.1016/j.atmosenv.2003.07.002.

[5] S.D. Ghude, D.M. Chate, C. Jena, G. Beig, R. Kumar, M.C. Barth, G.G. Pfister, S. Fadnavis, P. Pithani, Premature mortality in India due to $PM_{2.5}$ and ozone exposure, Geophys. Res. Lett. 43 (9) (2016) 4650–4658, https://doi.org/10.1002/2016GL068949.

[6] M. Jerrett, R.T. Burnett, C.A. Pope, K. Ito, G. Thurston, D. Krewski, Y. Shi, E. Calle, M. Thun, Long-Term ozone exposure and mortality, N. Engl. J. Med. 360 (11) (2009) 1085–1095, https://doi.org/10.1056/NEJMoa0803894.

[7] Y. Lin, F. Jiang, J. Zhao, G. Zhu, X. He, X. Ma, S. Li, C.E. Sabel, H. Wang, Impacts of O_3 on premature mortality and crop yield loss across China, Atmos. Environ. 194 (2018) 41–47, https://doi.org/10.1016/j.atmosenv.2018.09.024.

[8] B. Sinha, K. Sangwan, Y. Maurya, V. Kumar, C. Sarkar, B.P. Chandra, V. Sinha, Assessment of crop yield losses in Punjab and Haryana using 2 years of continuous in situ ozone measurements, Atmos. Chem. Phys. 15 (2015) 9555–9576, https://doi.org/10.5194/acp-15-9555-2015.

[9] R.K. Pachauri, M.R. Allen, V.R. Barros, J. Broome, W. Cramer, R. Christ, J.A. Church, L. Clarke, Q. Dahe, P. Dasgupta, N.K. Dubash, O. Edenhofer, I. Elgizouli, C.B. Field, P. Forster, P. Friedlingstein, J. Fuglestvedt, L. Gomez-Echeverri, S. Hallegatte, G. Hegerl, M. Howden, K. Jiang, B. Jimenez Cisneroz, V. Kattsov, H. Lee, K.J. Mach, J. Marotzke, M.D. Mastrandrea, L. Meyer, J. Minx, Y. Mulugetta, K. O'Brien, M. Oppenheimer, J.J. Pereira, R. Pichs-Madruga, G.-K. Plattner, H.-O. Pörtner, S.B. Power, B. Preston, N.H. Ravindranath, A. Reisinger, K. Riahi, M. Rusticucci, R. Scholes, K. Seyboth, Y. Sokona, R. Stavins, T.F. Stocker, P. Tschakert, D. van Vuuren, J.-P. van Ypserle, Climate Change 2014: Synthesis Report. Contribution of Working Groups I, II and III to the Fifth Assessment Report of the Intergovernmental Panel on Climate Change, Intergovernmental Panel on Climate Change, IPCC), Geneva, Switzerland, 2014.

[10] Y. Xue, S. Zhang, Z. Zhou, K. Wang, K. Liu, X. Wang, A. Shi, K. Xu, H. Tian, Spatio-temporal variations of multiple primary air pollutants emissions in Beijing of China, 2006–2015, Atmosphere 10 (9) (2019), https://doi.org/10.3390/atmos10090494.

[11] S. Li, J. Lang, Y. Zhou, X. Liang, D. Chen, P. Wei, Trends in ammonia emissions from light-duty gasoline vehicles in China, 1999–2017, Sci. Total Environ. 700 (2020) 134359, https://doi.org/10.1016/j.scitotenv.2019.134359.

[12] F. Liu, S. Beirle, Q. Zhang, R.J. van der A, B. Zheng, D. Tong, K. He, NO_x emission trends over Chinese cities estimated from OMI observations during 2005 to 2015, Atmos. Chem. Phys. 17 (15) (2017) 9261–9275, https://doi.org/10.5194/acp-17-9261-2017.

[13] G. Wang, J. Deng, Y. Zhang, Q. Zhang, L. Duan, J. Hao, J. Jiang, Air pollutant emissions from coal-fired power plants in China over the past two decades, Sci. Total Environ. 741 (2020) 140326, https://doi.org/10.1016/j.scitotenv.2020.140326.

[14] B. Zheng, D. Tong, M. Li, F. Liu, C. Hong, G. Geng, H. Li, X. Li, L. Peng, J. Qi, L. Yan, Y. Zhang, H. Zhao, Y. Zheng, K. He, Q. Zhang, Trends in China's anthropogenic emissions since 2010 as the consequence of clean air actions, Atmos. Chem. Phys. 18 (19) (2018) 14095–14111, https://doi.org/10.5194/acp-18-14095-2018.

[15] S. Cai, Y. Wang, B. Zhao, S. Wang, X. Chang, J. Hao, The impact of the "air pollution prevention and control action plan" on $PM_{2.5}$ concentrations in Jing-Jin-Ji region during 2012–2020, Sci. Total Environ. 580 (2017) 197–209, https://doi.org/10.1016/j.scitotenv.2016.11.188.

[16] H. Zhang, S. Wang, J. Hao, X. Wang, S. Wang, F. Chai, M. Li, Air pollution and control action in Beijing, J. Clean. Prod. 112 (2016) 1519–1527, https://doi.org/10.1016/j.jclepro.2015.04.092.

[17] Y. Wang, W. Gao, S. Wang, S. Tao, Z. Gong, D. Ji, L. Wang, Z. Liu, H. Yanfeng, S. Tian, J. Li, L. Mingge, Y. Yang, B. Chu, T. Petäjä, V.-M. Kerminen, H. He, J. Hao, Y. Zhang, Contrasting trends of $PM_{2.5}$ and surface-ozone concentrations in China from 2013 to 2017, Natl. Sci. Rev. 7 (2020), https://doi.org/10.1093/nsr/nwaa032.

[18] K. Li, J. Jacob Daniel, H. Liao, L. Shen, Q. Zhang, H. Bates Kelvin, Anthropogenic drivers of 2013–2017 trends in summer surface ozone in China, Proc. Natl. Acad. Sci. USA 116 (2) (2019) 422–427, https://doi.org/10.1073/

pnas.1812168116.
[19] Z. Ma, J. Xu, W. Quan, Z. Zhang, W. Lin, X. Xu, Significant increase of surface ozone at a rural site, north of eastern China, Atmos. Chem. Phys. 16 (6) (2016) 3969–3977, https://doi.org/10.5194/acp-16-3969-2016.
[20] X. Xu, W. Lin, W. Xu, J. Jin, Y. Wang, G. Zhang, X. Zhang, Z. Ma, Y. Dong, Q. Ma, D. Yu, Z. Li, D. Wang, H. Zhao, Long-term changes of regional ozone in China: implications for human health and ecosystem impacts, Elementa: Sci. Anthrop. 8 (2020), https://doi.org/10.1525/elementa.409.
[21] H. Han, J. Liu, L. Shu, T. Wang, H. Yuan, Local and synoptic meteorological influences on daily variability in summertime surface ozone in eastern China, Atmos. Chem. Phys. 20 (1) (2020) 203–222, https://doi.org/10.5194/acp-20-203-2020.
[22] H. Han, J. Liu, H. Yuan, B. Zhuang, Y. Zhu, Y. Wu, Y. Yan, A. Ding, Characteristics of intercontinental transport of tropospheric ozone from Africa to Asia, Atmos. Chem. Phys. 18 (6) (2018) 4251–4276, https://doi.org/10.5194/acp-18-4251-2018.
[23] T. Wang, L. Xue, P. Brimblecombe, Y.F. Lam, L. Li, L. Zhang, Ozone pollution in China: a review of concentrations, meteorological influences, chemical precursors, and effects, Sci. Total Environ. 575 (2017) 1582–1596, https://doi.org/10.1016/j.scitotenv.2016.10.081.
[24] E. Meyer, H. Schlünzen, The influence of emission changes on ozone concentrations and nitrogen deposition into the southern North Sea, Meteorol. Z. 20 (2011) 75–84, https://doi.org/10.1127/0941-2948/2011/0489.
[25] T. Liu, X. Wang, J. Hu, Q. Wang, J. An, K. Gong, J. Sun, L. Li, M. Qin, J. Li, J. Tian, Y. Huang, H. Liao, M. Zhou, Q. Hu, R. Yan, H. Wang, C. Huang, Driving forces of changes in air quality during the COVID-19 lockdown period in the Yangtze River Delta region, China, Environ. Sci. Technol. Lett. 7 (11) (2020) 779–786, https://doi.org/10.1021/acs.estlett.0c00511.
[26] X. Jin, T. Holloway, Spatial and temporal variability of ozone sensitivity over China observed from the Ozone Monitoring Instrument, J. Geophys. Res. 120 (14) (2015) 7229–7246, https://doi.org/10.1002/2015jd023250.
[27] S. Sillman, The relation between ozone, NO_x and hydrocarbons in urban and polluted rural environments, Atmos. Environ. 33 (12) (1999) 1821–1845, https://doi.org/10.1016/S1352-2310(98)00345-8.
[28] L. Ye, X. Wang, S. Fan, W. Chen, M. Chang, S. Zhou, Z. Wu, Q. Fan, Photochemical indicators of ozone sensitivity: application in the Pearl River Delta, China, Front. Environ. Sci. Eng. 10 (6) (2016), https://doi.org/10.1007/s11783-016-0887-1.
[29] A. Ding, X. Huang, C. Fu, Air Pollution and Weather Interaction in East Asia, Oxford University Press, 2017.
[30] S. Lou, H. Liao, Y. Yang, Q. Mu, Simulation of the interannual variations of tropospheric ozone over China: roles of variations in meteorological parameters and anthropogenic emissions, Atmos. Environ. 122 (2015) 839–851, https://doi.org/10.1016/j.atmosenv.2015.08.081.
[31] C. Gong, H. Liao, A typical weather pattern for ozone pollution events in North China, Atmos. Chem. Phys. 19 (22) (2019) 13725–13740, https://doi.org/10.5194/acp-19-13725-2019.
[32] X. Lu, L. Zhang, L. Shen, Meteorology and climate influences on tropospheric ozone: a review of natural sources, chemistry, and transport patterns, Curr. Pollut. Rep. 5 (4) (2019) 238–260, https://doi.org/10.1007/s40726-019-00118-3.
[33] Y. Dong, J. Li, J. Guo, Z. Jiang, Y. Chu, L. Chang, Y. Yang, H. Liao, The impact of synoptic patterns on summertime ozone pollution in the North China Plain, Sci. Total Environ. 735 (2020) 139559, https://doi.org/10.1016/j.scitotenv.2020.139559.
[34] L. Shen, L.J. Mickley, Seasonal prediction of US summertime ozone using statistical analysis of large scale climate patterns, Proc. Natl. Acad. Sci. USA 114 (10) (2017) 2491–2496, https://doi.org/10.1073/pnas.1610708114.
[35] T. Deng, T. Wang, S. Wang, Y. Zou, C. Yin, F. Li, L. Liu, N. Wang, L. Song, C. Wu, D. Wu, Impact of typhoon periphery on high ozone and high aerosol pollution in the Pearl River Delta region, Sci. Total Environ. 668 (2019), https://doi.org/10.1016/j.scitotenv.2019.02.450.
[36] J.-P. Huang, J.C.H. Fung, A.K.H. Lau, Y. Qin, Numerical simulation and process analysis of typhoon-related ozone episodes in Hong Kong, J. Geophys. Res. 110 (D5) (2005), https://doi.org/10.1029/2004JD004914.
[37] F. Jiang, T. Wang, T. Wang, M. Xie, H. Zhao, Numerical modeling of a continuous photochemical pollution episode in Hong Kong using WRF–chem, Atmos. Environ. 42 (2008) 8717–8727, https://doi.org/10.1016/j.atmosenv.2008.08.034.
[38] Y.C. Jiang, T.L. Zhao, J. Liu, X.D. Xu, C.H. Tan, X.H. Cheng, X.Y. Bi, J.B. Gan, J.F. You, S.Z. Zhao, Why does surface ozone peak before a typhoon landing in southeast China? Atmos. Chem. Phys. 15 (23) (2015) 13331–13338, https://doi.org/10.5194/acp-15-13331-2015.
[39] L. Shu, M. Xie, T. Wang, D. Gao, P. Chen, Y. Han, S. Li, B. Zhuang, M. Li, Integrated studies of a regional ozone pollution synthetically affected by subtropical high and typhoon system in the Yangtze River Delta region, China, Atmos. Chem. Phys. 16 (24) (2016) 15801–15819, https://doi.org/10.5194/acp-16-15801-2016.
[40] N. Wang, X. Huang, J. Xu, T. Wang, Z.-M. Tan, A. Ding, Typhoon-boosted biogenic emission aggravates cross-regional ozone pollution in China, Sci. Adv. 8 (2022), https://doi.org/10.1126/sciadv.abl6166.
[41] K. Ding, J. Liu, A. Ding, Q. Liu, T.L. Zhao, J. Shi, Y. Han, H. Wang, F. Jiang, Uplifting of carbon monoxide from biomass burning and anthropogenic sources to the free troposphere in East Asia, Atmos. Chem. Phys. 15 (5) (2015) 2843–2866, https://doi.org/10.5194/acp-15-2843-2015.
[42] G. Dufour, M. Eremenko, J. Cuesta, C. Doche, G. Foret, M. Beekmann, A. Cheiney, Y. Wang, Z. Cai, Y. Liu, M. Takigawa, Y. Kanaya, J.M. Flaud, Springtime daily variations in lower-tropospheric ozone over east Asia: the role of cyclonic activity and pollution as observed from space with IASI, Atmos. Chem. Phys. 15 (18) (2015) 10839–10856, https://doi.org/10.5194/acp-15-10839-2015.
[43] Z. Zhao, Y. Wang, Influence of the West Pacific subtropical high on surface ozone daily variability in summertime over eastern China, Atmos. Environ. 170 (2017) 197–204, https://doi.org/10.1016/j.atmosenv.2017.09.024.
[44] L. Shen, L.J. Mickley, A.P.K. Tai, Influence of synoptic patterns on surface ozone variability over the eastern United States from 1980 to 2012, Atmos. Chem. Phys. 15 (19) (2015) 10925–10938, https://doi.org/10.5194/acp-15-10925-2015.
[45] Y. Wang, B. Jia, S.C. Wang, M. Estes, L. Shen, Y. Xie, Influence of the Bermuda High on interannual variability of summertime ozone in the Houston–Galveston–Brazoria region, Atmos. Chem. Phys. 16 (23) (2016) 15265–15276, https://doi.org/10.5194/acp-16-15265-2016.
[46] H. Guo, Z.H. Ling, K. Cheung, F. Jiang, D.W. Wang, I.J. Simpson, B. Barletta, S. Meinardi, T.J. Wang, X.M. Wang, S.M. Saunders, D.R. Blake, Characterization of photochemical pollution at different elevations in mountainous areas in Hong Kong, Atmos. Chem. Phys. 13 (8) (2013) 3881–3898, https://doi.org/10.5194/acp-13-3881-2013.
[47] X. Lu, K.-C. Chow, T. Yao, A.K.H. Lau, J.C.H. Fung, Effects of urbanization on the land sea breeze circulation over the Pearl River Delta region in winter, Int. J. Climatol. 30 (7) (2010) 1089–1104, https://doi.org/10.1002/joc.1947.
[48] H. Wang, X. Lyu, H. Guo, Y. Wang, S. Zou, Z. Ling, X. Wang, F. Jiang, Y. Zeren, W. Pan, X. Huang, J. Shen, Ozone pollution around a coastal region of South China Sea: interaction between marine and continental air, Atmos. Chem. Phys. 18 (6) (2018) 4277–4295, https://doi.org/10.5194/acp-18-4277-2018.
[49] C.-H. Lin, C.-H. Lai, Y.-L. Wu, P.-H. Lin, H.-C. Lai, Impact of sea breeze air masses laden with ozone on inland surface ozone concentrations: a case study of the northern coast of Taiwan, J. Geophys. Res. 112 (D14) (2007), https://doi.org/10.1029/2006JD008123.
[50] A. Ding, T. Wang, M. Zhao, T. Wang, Z. Li, Simulation of sea-land breezes and a discussion of their implications on the transport of air pollution during a multi-day ozone episode in the Pearl River Delta of China, Atmos. Environ. 38 (39) (2004) 6737–6750, https://doi.org/10.1016/j.atmosenv.2004.09.017.
[51] I.-B. Oh, Y.-K. Kim, H.w. Lee, C.-H. Kim, An observational and numerical study of the effects of the late sea breeze on ozone distributions in the Busan metropolitan area, Korea, Atmos. Environ. 40 (7) (2006) 1284–1298, https://doi.org/10.1016/j.atmosenv.2005.10.049.
[52] M.M. Millán, E. Mantilla, R. Salvador, A. Carratalá, M.J. Sanz, L. Alonso, G. Gangoiti, M. Navazo, Ozone cycles in the western mediterranean basin: interpretation of monitoring data in complex coastal terrain, J. Appl. Meteorol. Climatol. 39 (4) (2000) 487–508, https://doi.org/10.1175/1520-0450(2000)039<0487:OCITWM>2.0.CO;2.
[53] C.-H. Lin, Y.-L. Wu, C.-H. Lai, P.-H. Lin, H.-C. Lai, P.-L. Lin, Experimental investigation of ozone accumulation overnight during a wintertime ozone episode in south Taiwan, Atmos. Environ. 38 (26) (2004) 4267–4278, https://doi.org/10.1016/j.atmosenv.2004.05.003.
[54] D. Boucouvala, R. Bornstein, Analysis of transport patterns during an SCOS97-NARSTO episode, Atmos. Environ. 37 (2003) 73–94, https://doi.org/10.1016/S1352-2310(03)00383-2.
[55] Y. Zheng, F. Jiang, S. Feng, Z. Cai, Y. Shen, C. Ying, X. Wang, Q. Liu, Long-range transport of ozone across the eastern China seas: a case study in coastal cities in southeastern China, Sci. Total Environ. 768 (2021) 144520, https://doi.org/10.1016/j.scitotenv.2020.144520.
[56] M.M. Millán, M. José Sanz, R. Salvador, E. Mantilla, Atmospheric dynamics and ozone cycles related to nitrogen deposition in the western Mediterranean, Environ. Pollut. 118 (2) (2002) 167–186, https://doi.org/10.1016/S0269-7491(01)00311-6.
[57] F. Cousin, P. Tulet, R. Rosset, Interaction between local and regional pollution during Escompte 2001: impact on surface ozone concentrations (IOP2a and 2b), Atmos. Res. 74 (1) (2005) 117–137, https://doi.org/10.1016/j.atmosres.2004.04.012.
[58] F. Jiang, H. Guo, T.J. Wang, H.R. Cheng, X.M. Wang, I.J. Simpson, A.J. Ding, S.M. Saunders, S.H.M. Lam, D.R. Blake, An ozone episode in the Pearl River Delta: field observation and model simulation, J. Geophys. Res. 115 (D22) (2010), https://doi.org/10.1029/2009JD013583.
[59] G. Li, N. Bei, J. Cao, R. Huang, J. Wu, T. Feng, Y. Wang, S. Liu, Q. Zhang, X. Tie, L.T. Molina, A possible pathway for rapid growth of sulfate during haze days in China, Atmos. Chem. Phys. 17 (5) (2017) 3301–3316, https://doi.org/10.5194/acp-17-3301-2017.
[60] G. Li, N. Bei, J. Cao, J. Wu, X. Long, T. Feng, W. Dai, S. Liu, Q. Zhang, X. Tie, Widespread and persistent ozone pollution in eastern China during the non-winter season of 2015: observations and source attributions, Atmos. Chem. Phys. 17 (4) (2017) 2759–2774, https://doi.org/10.5194/acp-17-2759-2017.
[61] D. Tong, Q. Zhang, S.J. Davis, F. Liu, B. Zheng, G. Geng, T. Xue, M. Li, C. Hong, Z. Lu, D.G. Streets, D. Guan, K. He, Targeted emission reductions from global super-polluting power plant units, Nat. Sustain. 1 (1) (2018) 59–68, https://doi.org/10.1038/s41893-017-0003-y.
[62] T. Xiong, W. Jiang, W. Gao, Current status and prediction of major atmospheric emissions from coal-fired power plants in Shandong Province, China, Atmos. Environ. 124 (2016) 46–52, https://doi.org/10.1016/j.atmosenv.2015.11.002.
[63] S. Liu, D. Wang, Z. Chen, L. Bai, J. Zhang, Y. Huang, Analysis on the

characteristics and trend of ozone pollution in circum-Bohai-Sea Zone, Environ. Sci. Technol. (s1) (2018), https://doi.org/10.19672/j.cnki.1003-6504.2018.S1.047.
[64] Q. Zhang, Study on the effect of atmospheric ozone concentration in DaLian city by exogenous ozone input from Bohai Bay, Heilongjiang Environ. J. 40 (2) (2016) 75–78, https://doi.org/10.3969/j.issn.1674-263X.2016.02.028.
[65] MEP, Technical specifications for operation and quality control of ambient air quality continuous automated monitoring system for SO_2, NO_2, O_3 and CO, Beijing, in: Ministry of Environmental Protection of the People's Republic of China, 2018.
[66] MEP, Technical regulation for selection of ambient air quality monitoring stations (on trial), Beijing, in: Ministry of Environmental Protection of the People's Republic of China, 2013.
[67] W.C. Skamarock, J.B. Klemp, J. Dudhia, D.O. Gill, Z. Liu, J. Berner, W. Wang, J.G. Powers, M.G. Duda, D. Barker, X.-y. Huang, A Description of the Advanced Research WRF Model Version 4, University Corporation for Atmospheric Research, Boulder, Colorado, USA, 2019.
[68] D. Byun, K.L. Schere, Review of the governing equations, computational algorithms, and other components of the models-3 community Multiscale air quality (CMAQ) modeling system, Appl. Mech. Rev. 59 (2) (2006) 51–77, https://doi.org/10.1115/1.2128636.
[69] J. Yang, K. Duan, Effects of initial drivers and land use on WRF modeling for near-surface fields and atmospheric boundary layer over the northeastern Tibetan plateau, 2016, Adv. Meteorol. (2016) 7849249, https://doi.org/10.1155/2016/7849249.
[70] A. Guenther, X. Jiang, C. Heald, T. Sakulyanontvittaya, T. Duhl, L. Emmons, X. Wang, The Model of Emissions of Gases and Aerosols from Nature Version 2.1 (MEGAN2.1): an extended and updated framework for modeling biogenic emissions, Geosci. Model Dev. (GMD) 5 (2012) 1471–1492, https://doi.org/10.5194/gmd-5-1471-2012.
[71] M. Li, H. Liu, G. Geng, C. Hong, F. Liu, Y. Song, D. Tong, B. Zheng, H. Cui, H. Man, Q. Zhang, K. He, Anthropogenic emission inventories in China: a review, Natl. Sci. Rev. 4 (6) (2017) 834–866, https://doi.org/10.1093/nsr/nwx150.
[72] M. Li, Q. Zhang, J.I. Kurokawa, J.H. Woo, K. He, Z. Lu, T. Ohara, Y. Song, D.G. Streets, G.R. Carmichael, Y. Cheng, C. Hong, H. Huo, X. Jiang, S. Kang, F. Liu, H. Su, B. Zheng, MIX: a mosaic Asian anthropogenic emission inventory under the international collaboration framework of the MICS-Asia and HTAP, Atmos. Chem. Phys. 17 (2) (2017) 935–963, https://doi.org/10.5194/acp-17-935-2017.
[73] H. Liu, Z.-H. Meng, Z.-F. Lv, X.-T. Wang, F.-Y. Deng, Y. Liu, Y.-N. Zhang, M.-S. Shi, Q. Zhang, K.-B. He, Emissions and health impacts from global shipping embodied in US–China bilateral trade, Nat. Sustain. 2 (11) (2019) 1027–1033, https://doi.org/10.1038/s41893-019-0414-z.
[74] X. Wang, H. Liu, Z. Lv, F. Deng, H. Xu, L. Qi, M. Shi, J. Zhao, S. Zheng, H. Man, K. He, Trade-linked shipping CO2 emissions, Nat. Clim. Change 11 (11) (2021) 945–951, https://doi.org/10.1038/s41558-021-01176-6.
[75] H. Liu, M. Fu, X. Jin, Y. Shang, D. Shindell, G. Faluvegi, C. Shindell, K. He, Health and climate impacts of ocean-going vessels in East Asia, Nat. Clim. Change 6 (11) (2016) 1037–1041, https://doi.org/10.1038/nclimate3083.
[76] X. Wang, W. Yi, Z. Lv, F. Deng, S. Zheng, H. Xu, J. Zhao, H. Liu, K. He, Ship emissions around China under gradually promoted control policies from 2016 to 2019, Atmos. Chem. Phys. 21 (18) (2021) 13835–13853, https://doi.org/10.5194/acp-21-13835-2021.
[77] D. Byun, J. Ching, Science Algorithms of the EPA Models-3 Community Multiscale Air Quality (CMAQ) Modeling System, U.S. Environmental Protection Agency, Washington, DC, 1999, pp. 1–15.
[78] T.-F. Chen, K.-H. Chang, C.-H. Lee, Simulation and analysis of causes of a haze episode by combining CMAQ-IPR and brute force source sensitivity method, Atmos. Environ. 218 (2019) 117006, https://doi.org/10.1016/j.atmosenv.2019.117006.
[79] M. Gonçalves, P. Jiménez-Guerrero, J.M. Baldasano, Contribution of atmospheric processes affecting the dynamics of air pollution in South-Western Europe during a typical summertime photochemical episode, Atmos. Chem. Phys. 9 (3) (2009) 849–864, https://doi.org/10.5194/acp-9-849-2009.
[80] W. Jeon, Y. Choi, H.W. Lee, S.-H. Lee, J.-W. Yoo, J. Park, H.-J. Lee, A quantitative analysis of grid nudging effect on each process of $PM_{2.5}$ production in the Korean Peninsula, Atmos. Environ. 122 (2015) 763–774, https://doi.org/10.1016/j.atmosenv.2015.10.050.
[81] W.-B. Jeon, S.-H. Lee, H.-W. Lee, H.-G. Kim, Process analysis of the impact of atmospheric recirculation on consecutive high-O_3 episodes over the Seoul Metropolitan Area in the Korean Peninsula, Atmos. Environ. 63 (2012) 213–222, https://doi.org/10.1016/j.atmosenv.2012.09.031.
[82] L. Li, C. Chen, C. Huang, H. Huang, G.-f. Zhang, Y. Wang, H. Wang, S. Lou, L. Qiao, M. Zhou, M. Chen, Y. Chen, J. Fu, D. Streets, C. Jang, Process analysis of regional ozone formation over the Yangtze River Delta, China using the community multi-scale air quality modeling system, ACPD 12 (2012) 15049–15082, https://doi.org/10.5194/acpd-12-15049-2012.
[83] X.-H. Liu, Y. Zhang, Understanding of the formation mechanisms of ozone and particulate matter at a fine scale over the southeastern U.S.: process analyses and responses to future-year emissions, Atmos. Environ. 74 (2013) 259–276, https://doi.org/10.1016/j.atmosenv.2013.03.057.
[84] J. Jung, Y. Choi, A.H. Souri, A. Mousavinezhad, A. Sayeed, K. Lee, The impact of springtime-transported air pollutants on local air quality with satellite-constrained NO x emission adjustments over East Asia, J. Geophys. Res. Atmos. 127 (2022), https://doi.org/10.1029/2021JD035251.
[85] Y. Kaore, R. Pedruzzi, E. Galvão, I. Araújo, T. Alburquerque, P. Kumar, E.G. Sperandio Nascimento, D. Moreira, Source apportionment modelling of $PM_{2.5}$ using CMAQ-ISAM over a tropical coastal-urban area, Atmos. Pollut. Res. 12 (2021) 101250, https://doi.org/10.1016/j.apr.2021.101250.
[86] R.H.F. Kwok, K.R. Baker, S.L. Napelenok, G.S. Tonnesen, Photochemical grid model implementation and application of VOC, NO_x, and O_3 source apportionment, Geosci. Model Dev. (GMD) 8 (1) (2015) 99–114, https://doi.org/10.5194/gmd-8-99-2015.
[87] R.H.F. Kwok, S.L. Napelenok, K.R. Baker, Implementation and evaluation of $PM_{2.5}$ source contribution analysis in a photochemical model, Atmos. Environ. 80 (2013) 398–407, https://doi.org/10.1016/j.atmosenv.2013.08.017.
[88] Y. Lu, J. Chi, L. Yao, L. Yang, W. Li, Z. Wang, W. Wang, Composition and mixing state of water soluble inorganic ions during hazy days in a background region of North China, Sci. China Earth Sci. 58 (11) (2015) 2026–2033, https://doi.org/10.1007/s11430-015-5131-5.
[89] S.L. Napelenok, R. Vedantham, P.V. Bhave, G.A. Pouliot, R.H.F. Kwok, Source-receptor reconciliation of fine-particulate emissions from residential wood combustion in the southeastern United States. Atmos, Environ. Times 98 (2014) 454–460, https://doi.org/10.1016/j.atmosenv.2014.09.021.
[90] H. Chen, Y. Chen, D. Li, W. Li, Y. Yang, Identifying water vapor sources of precipitation in forest and grassland in the north slope of the Tianshan Mountains, Central Asia, J. Arid Land 14 (3) (2022) 297–309, https://doi.org/10.1007/s40333-022-0090-0.
[91] R.R. Draxier, G. Hess, An overview of the HYSPLIT_4 modeling system of trajectories, dispersion, and deposition, Aust. Meteorol. Mag. 47 (1998) 295–308.
[92] MEP, Ambient air quality standards of China, Beijing, in: Ministry of Environmental Protection of the People's Republic of China, 2012.
[93] M. Xie, K. Zhu, T. Wang, P. Chen, Y. Han, S. Li, B. Zhuang, L. Shu, Temporal characterization and regional contribution to O_3 and NO_x at an urban and a suburban site in Nanjing, China, Sci. Total Environ. 551–552 (2016) 533–545, https://doi.org/10.1016/j.scitotenv.2016.02.047.
[94] B. Zhu, H. Kang, T. Zhu, J. Su, X. Hou, J. Gao, Impact of Shanghai urban land surface forcing on downstream city ozone chemistry, J. Geophys. Res. 120 (9) (2015) 4340–4351, https://doi.org/10.1002/2014jd022859.